ORIGINAL RESEARCH ARTICLE

Slag Flow in the Packed Bed With Varied Properties and Bed Conditions: Numerical Investigation

X.F. DONG, A. JAYASEKARA, D. SERT, R. FERREIRA, P. GARDIN, S.J. CHEW, D. PINSON, B.J. MONAGHAN, and P. ZULLI

Molten slag, which is primarily generated in the blast furnace (BF) cohesive zone, trickles down through the coke packed bed in the form of films, rivulets, or droplets in the lower zone of the BF. During its downward flow, there are significant interactions occurring between slag and other phases such as gas, coke particles, hot metal, and fine powders. In terms of these interactions, slag flow behavior can greatly affect BF productivity and be associated with furnace irregularities such as channeling, hanging, and slipping. Hence, understanding the interactions between phases is useful to maximizing BF efficiency in terms of operating cost, reliability, and production capacity. In the current study, a Volume of Fluid (VOF) modeling technique was applied to track the movement of individual slag droplets in the packed bed at a mesoscopic level, considering various bed permeabilities, more wide-ranging slag properties, and different wettability between slag and packing particles. Results demonstrate the significant role of modeling at a mesoscopic level in understanding macroscopic slag flow behavior. Modeling work helps to visualize the trickling behavior of slag droplets in more realistic and complex conditions representing a BF, and clarify the mechanisms of the different flow patterns generated for variations in operating conditions. Transient flow characteristics such as localized slag accumulation and droplet morphology were identified and analyzed in relation to complex condition changes. The current modeling proved to be a valuable tool to provide a foundation for better understanding the slag flow behavior and its interactions with other phases in the BF lower zone.

https://doi.org/10.1007/s11663-022-02685-1

I. INTRODUCTION

MOLTEN slag forms in the softening-melting zone of an ironmaking blast furnace (BF) and then trickles through the coke packed bed before being discharged from the taphole, together with hot metal.[1,2] The formation and dripping of slag have a significant impact on the BF operation in terms of furnace permeability, fuel consumption, process stability, product quality, and productivity.[3,4]

The composition of the initial slag formed in the cohesive zone, often referred to as primary slag, varies in relation to charged materials, such as sinter, lump ore, or pellets. In particular, the iron oxide (FeO) content in primary slag may range up to 30 pct.[3,5–7] As slag flows through the coke packed bed in the form of films, rivulets, or droplets, *i.e.,* a typical trickle flow,[8] its composition changes through reduction of metallic oxides, as well as slag assimilation of mineral matter from coke and remnant char from the combustion and gasification of pulverized coal. The slag composition will inevitably vary in the lower zone, both radially and vertically, such that the primary slag gradually transforms to bosh slag and ultimately to a final slag composition representative of the hearth slag.[3] In addition to this, the operating conditions in the furnace, such as the temperature distribution and the coke particle surfaces,[9] vary along the slag flow path. Hence, understanding slag flow behavior in the lower zone is

X.F. DONG, A. JAYASEKARA, B.J. MONAGHAN, and P. ZULLI are with the School of Mechanical, Materials, Mechatronic and Biomedical Engineering, University of Wollongong, Wollongong, NSW, 2522, Australia and also with the ARC Research Hub for Australian Steel Innovation, University of Wollongong, Wollongong, NSW 2522, Australia. Contact e-mail: xuefeng.dong@uow.edu.au D. SERT, R. FERREIRA, and P. GARDIN are with the ARC Research Hub for Australian Steel Innovation, University of Wollongong and also with the ArcelorMittal Maizieres Research SA, 57283 Maizéres-Lés-Metz, France. S.J. CHEW and D. PINSON are with the ARC Research Hub for Australian Steel Innovation, University of Wollongong and also with the Coke & Ironmaking Technology, BlueScope Ltd, Wollongong, NSW 2522, Australia.

Manuscript submitted May 2, 2022; accepted October 15, 2022.
Article published online November 23, 2022.

critical for designing optimal BF operations particularly when striving for high production and pulverized coal rate (PCR).[5]

There have been a number of important observations reported in relation to slag phenomena in the lower zone. For example, through examination of samples from previous BF dissection studies (*e.g.*,[2]), "icicles" with deposited slag were observed within or near the softening-melting zone, which is a unique flow pattern. Furthermore, tuyere-probe samples showed indefinite-shaped slag droplets existing at tuyere level,[5] possibly indicating variable slag flow behavior as it trickles through the bed. To better understand the slag flow behavior through the lower zone coke bed, a number of low temperature (LT) experiments[10–20] have been carried out using different aqueous solutions of inorganic compounds and uncoated/coated particles. Through these studies, typical liquid flow behaviors were clarified such as liquid channeling,[19,21] flow deviation caused by gas phase,[22] and dispersion in the packed bed.[23,24] However, the aqueous solutions used in these LT experiments are unlikely to adequately simulate precisely the key features of molten slag flow.[25] In terms of wettability, the surface tension of slag is significantly different from those of aqueous solutions, and the interfacial tension between slag and carbonaceous materials in the high temperature condition cannot be fully replicated in LT experiments. In particular, sessile drop experiments show that the contact angle may significantly change when reaction occurs at the interface between slag and coke particles.[26,27] The change may become more evident as the temperature increases.[1] Thus, in recent studies,[25,27–34] slags with compositions similar to the BF were used in high temperature (HT) experiments, some involving laboratory-scale, coke packed beds. From these studies, estimates of slag holdup in a coke bed were obtained. These estimates highlighted the differences between LT and HT experimental results.[25,32]

With improved computational capacity and high performance computing, a number of numerical investigations of slag flow in a coke packed bed have been recently carried out at the mesoscopic level.[30,35–47] These models require fewer assumptions and empirical correlations compared to previous numerical work undertaken at the macroscopic level.[24,48–53] Typically, numerical techniques such as Smooth Particle Hydrodynamic[54,55] and Volume of Fluid (VOF)[56] were applied to track the liquid droplets movement through the packed bed at a mesoscopic level. Both approaches have been applied to investigate single- and binary-liquid flow in the packed bed.[30,35–47] The results show that the trajectory of liquid droplets can be tracked, providing detailed information about the interaction between liquid droplets and particles. These approaches also demonstrate their potential application[45] for situations where strong gas interactions, and heat and mass transfer occur.

In order to achieve higher levels of PCR and BF productivity, the controllable range and potential irregularity of slag flow have to be better estimated and predicted. Moreover, with the urgency to reduce greenhouse gas emissions globally, the BF ironmaking process has to adapt to the possible changes in burden materials and injection conditions. All these changes bring some level of risk and uncertainty to the furnace operation, and hence, a better understanding of slag flow behavior associated with the critical conditions is required.

Therefore, in this study, a numerical model based on the VOF approach was applied to investigate the slag flow behavior, considering more realistic and complex conditions such as varying bed permeability and wide-ranging slag properties. This paper is arranged in the following order. First, wetting and non-wetting slag flow in the uniform packed bed was investigated. Then, slag flow in the bed with different poor permeability regions was studied. Finally, high viscosity slag flow behaviors in different bed structures were compared.

II. MATHEMATICAL MODELING AND BOUNDARY CONDITIONS

A. *Governing Equations and Methodologies*

The Volume of Fluid (VOF) method developed and validated previously[36,47] was applied to simulate the slag flow in a coke packed bed. The general governing equations for mass and momentum transfer, and the relevant assumptions for slag flow were given in recent publications[36,47] and briefly summarized in Table I. Computations were carried out using the ANSYS-Fluent (v19.1) platform.

The following assumptions were imposed for the mathematical modeling.

- Incompressible multiphase flow
- No mass transfer between phases
- No variations in the surface tension coefficient
- Phases are immiscible with a clearly defined interface
- The system is in a thermal equilibrium
- Phases share the same velocity field
- Laminar flow

The methodologies adopted in the simulation are summarized in Table II.

B. *Computational Domain and Material Properties*

Two-dimensional simulations were carried out of slag flow in a HT experimental packed bed geometry: the base bed previously described[47] and two other packed bed set-ups with poor permeability regions. A Cartesian coordinate system was used. For the base bed, the packing particles were assumed to be spherical with a diameter of 10 mm and evenly distributed in the bed to give a bed porosity of 0.51.

Figure 1(a) shows the computational domain for the base bed. The inlet, outlet, wall, and symmetric lines are highlighted via different colors, *i.e.*, red, green, black, and light green, respectively. The space below the packed bed was also considered in the simulation to avoid the effect of the outlet on the numerical results.

Table I. Governing Equations

Equations	Descriptions
Continuity	$\frac{\partial \varepsilon_i}{\partial t} + \nabla \cdot (\varepsilon_i \boldsymbol{u}) = 0$ (1)
Momentum	$\frac{\partial}{\partial t}(\rho \boldsymbol{u}) + \nabla \cdot (\rho \boldsymbol{u}\boldsymbol{u}) = -\nabla p + \nabla \cdot \tau + \rho \boldsymbol{g} + \boldsymbol{F}$ (2)
	$\boldsymbol{\tau} = \mu \left[\nabla \boldsymbol{u} + (\nabla \boldsymbol{u})^T \right]$ (3)
	$\boldsymbol{F} = 2\rho\kappa_i\sigma_{ij}\nabla\varepsilon_i/(\rho_i + \rho_j)$ in case of two phases (4)
	$\kappa_i = \nabla \cdot (\nabla\varepsilon_i/\lvert\nabla\varepsilon_i\rvert)$ (5)

Table II. Methodologies Used in the Simulation

Items	Schemes
Body Force	implicitly treated[57]
Discretization of Convective Terms	second order upwind scheme
Gradient Used to Discretize the Convection and Diffusion Terms	Green-Gauss node based treatment[58]
Velocity–Pressure Coupling	SIMPLE algorithm
Calculation of the Volume Fraction	implicit formulation
Temporal Derivation	bounded second order implicit
Calculation of Face Fluxes	modified HRIC

Figures 1(b) and (c) show the 2D computational domains for the beds with central and deadman-shaped poor permeability regions, respectively. Note that deadman refers to the quasi-stagnant core region of coke in the lower part of blast furnace.[1] In general, the bed permeability is a function of bed porosity, particle size, and shape.[57] The permeability increases with increasing particle size and bed porosity. In this study, only particle size, d_s, is changed to achieve permeability changes. Particles in the central region [Figure 1(b)] and deadman region [Figure 1(c)] are changed to 5 mm diameter, with the porosity remaining unchanged cf. the base bed condition.

Considering an intrinsic difference between two- and three-dimensional conditions, *i.e.,* non-identical pathways between 2 and 3D conditions, the current simulation results should be considered for qualitative analysis.

In this study, the base slag previously used in the experimental study[32] was applied. This is a typical SiO_2-MgO-CaO–Al_2O_3 quaternary slag. The properties of slag are given in Table III. Surface tension and density were calculated via NPL models,[59] and viscosity via the Riboud[60] model.

In the BF, the slag viscosity and contact angle with carbonaceous materials may vary significantly. The effect of these two key properties on flow behavior will be investigated in subsequent sections. In Sections III–A and III–B, four contact angles between slag and particle surface, 157, 120, 90, and 60 deg, were considered, representing a transition from non-wetting to wetting slag condition. The value of 157 deg (a relatively non-wetting condition) was based on recent sessile drop measurements undertaken by the authors for a slag-graphite system. The value of 60 deg represents a relatively wetting condition in the case of slag-coke/mineral matter reaction,[27,33,61] while 120 and 90 deg contact angles represent variations in wettability between non-wetting and wetting cases.

For the upper and lower wall surfaces, the slag wettability was considered to be completely non-wetting, *i.e.,* a contact angle of 180 deg.

In Section III–B–3, changing the slag viscosity from the base value (calculated as 0.264 Pa s) to four times this value (1.056 Pa s) was investigated. The latter value represents possible impacts on viscosity of slag, such as the effect of fines on the effective viscosity and/or slag subjected to lower temperatures in the lower zone.

C. *Initial and Boundary Conditions*

1. *Initial condition*

At the beginning of a simulation for each packed bed geometry, a slag region was patched near the inlet in the computational domain. The patch was initialized with a volume fraction set to unity for the slag phase and a zero velocity. Figure 2 shows the initial slag conditions for each packed bed. Each initial condition corresponds to the mass of slag that would flow into the bed within a period of 0.5 s.

2. *Inlet condition*

In the simulations, a periodic inlet condition was used for slag flow in the packed bed. The slag is periodically fed into the packed bed from four inlets at the top. The inlet slag velocity was set to be 5 mm s^{-1} with reference to the treatment in the literature.[35] The slag is fed into the bed in the following manner:

- In each time period of 0.75 second, slag is added to the bed in the first 0.5 second
- For each inlet, only 80 pct of the inlet area is used for slag flow
- The position of the slag inlet area, *i.e.,* 80 pct of each inlet, randomly changes every 0.75 second, attempt-

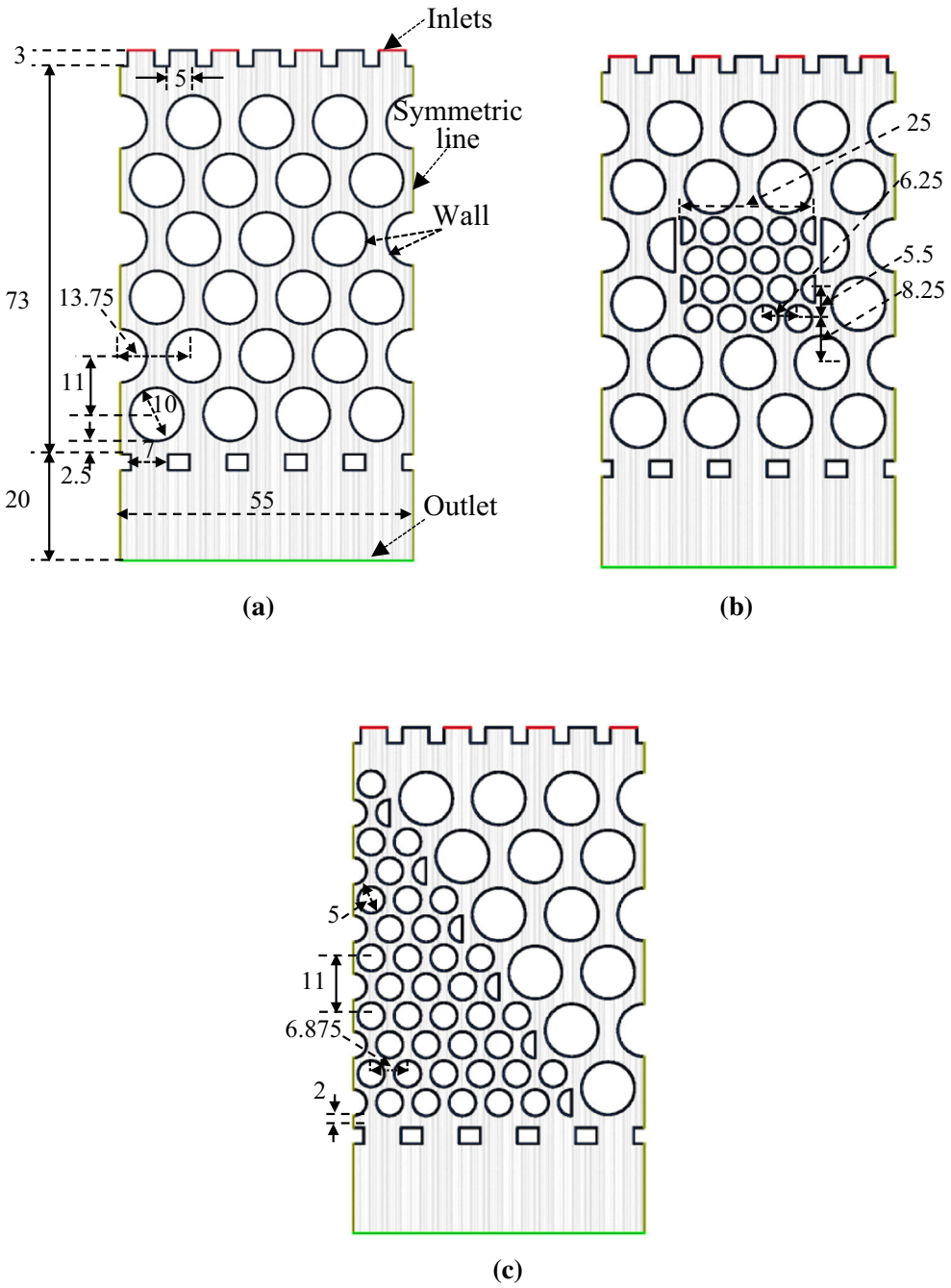

Fig. 1—2-D computational domain for slag flow in the packed bed (unit: mm): (*a*) base bed; (*b*) bed with central region of poor permeability; and (*c*) bed with deadman-shaped poor permeability region.

ing to reflect the uncertainty of slag droplet generation in practice

Through the above treatment, within every 0.75 second, slag droplets with an equivalent diameter of ~ 3.5 mm can be generated, which is based on estimations in the literature.[53] Note that the normalized random number, (float) rand()/RAND_MAX, was used to help implement the random variation of slag inlet location via a ANSYS-Fluent user-defined function, providing a comparable feed distribution between cases.

3. *Wall*

For the walls, a no-slip boundary condition was imposed for the slag velocities. The effect of wall adhesion at phase interfaces in contact with the wall boundary can be estimated considering the contact angle of slag at the wall θ_{iw} in the evaluation of the interfacial curvature near the wall. This is described by

$$\kappa_i = \nabla \cdot (\hat{n}_{iw} \cos\theta_{iw} + \hat{t}_{iw} \sin\theta_{iw}) \quad [6]$$

where $\hat{n}_{iw}$ and $\hat{t}_{iw}$ are the unit vector normal and tangential to the wall.

Table III. Properties of Base Slag Used in the Simulation

Liquid	Composition, Wt Pct				Viscosity, μ, Pa·s	Surface Tension, σ, N·m^{-1}	Density, ρ, kg·m^{-3}	T, °C
	CaO	SiO_2	Al_2O_3	MgO				
Slag	40.7	37.4	12.5	8.8	0.264	0.493	2675	1500

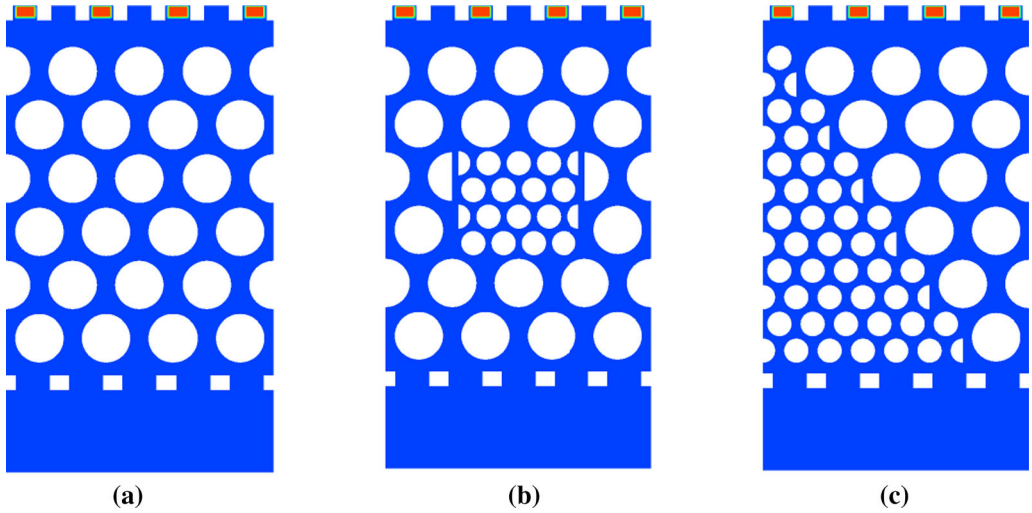

Fig. 2—Initial slag conditions in (*a*) base bed; (*b*) bed with central region of poor permeability; and (*c*) bed with deadman-shaped poor permeability region.

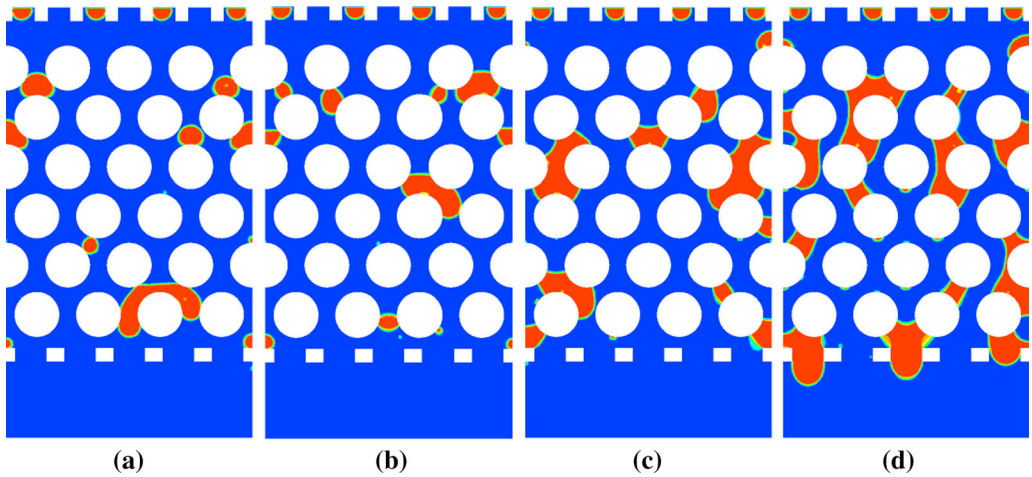

Fig. 3—Simulated slag flow in the packed bed at time t = 18 s for different contact angles: (*a*) 157 deg, (*b*) 120 deg, (*c*) 90 deg, and (*d*) 60 deg.

4. *Outlet*

A pressure outlet boundary condition was used for the outlet at the bottom of the packed bed.

III. RESULTS AND DISCUSSION

A. *Slag Flow in the Base Packed Bed with Different Wettability*

Figure 3 shows the slag flow fields at time t = 18 seconds for different contact angles in the base packed bed condition. Note that each computational case has run for 18 seconds, which is based on a quasi-steady state result being attained for the base slag condition. As mentioned, the contact angle change from 157 to 60 deg simulates the influence of non-wetting and wetting conditions, which characterize the relation between adhesive and cohesive forces acting, and reflects reactions that may occur at the coke particle surface.

As the contact angle (θ) between slag and the solid particle surface decreases, *i.e.,* characteristic of an increased adhesive force between slag and solid particles, the trickle flow of slag in the packed bed slows down. Compared to the non-wetting condition (θ = 157 deg), the wetting condition (θ = 60 deg) shows different flow behavior and slag holdup

distributions. The simulation results suggest that a non-wetting slag is likely to accumulate in the upper part of the bed. Once the hydrostatic pressure is sufficiently high, the slag can overcome the bed resistance and trickle through the lower part of the bed quite easily. On the other hand, a wetting slag is likely to accumulate throughout the packed bed and an evident creeping flow can be formed. It is estimated that the contact area between slag and solid particles may increase if the slag condition is more wetting.

Based on the simulated results, detailed information such as slag volume fraction, droplet characteristics (*e.g.,* size and shape), and contact length between slag and packing particle can be obtained.

1. *Variation of slag volume fraction*

Figure 4 shows the variation of total slag volume fraction in the packed particle region. In the early stages, a gradual increase in slag volume fraction indicates an accumulation of slag in the packed bed. Among the four different wetting conditions, the flow of the more non-wetting slag (θ = 157 deg) is the smoothest such that the earliest drop in volume fraction occurs at ~ 5 seconds (due to a large liquid droplet flowing out of bed) and the overall slag volume fraction is the lowest. In comparison, the more wetting slag (θ = 60 deg) has the highest total volume fraction, and the first significant change in volume fraction occurs at ~ 10 seconds. Within the computational time period of 18 seconds, there appears to be no clear difference in the total slag volume fraction trends for the other two slags (θ = 120 and 90 deg). Note that during those periods with positive changes of slag volume fraction, the similar slopes reflect slag continuously being fed into the bed, and only a small amount of slag is flowing out of the bed.

2. *Variations of slag circularity*

In the packed bed, slag droplets/rivulets have, for the majority of the time, indefinite shapes. This means that as droplets flow through gaps between particles, or squeeze into gaps, non-spherical deformed shapes are formed. This is particularly true for a more wetting slag. Interestingly, Ichida *et al.*[5] report results from tuyere sampling probes that showed solidified slag of different shapes: (1) blocked-shaped slag, possibly representing slag with high residence time in the furnace; and, in contrast, (2) indefinite-shaped slag, possibly representing dripping slag, *i.e.,* dynamic slag holdup when operating a BF.

In considering the current numerical results, such as those shown in Figure 3, there is uncertainty regarding the representativeness of indefinite-shaped slag droplets/rivulets within the bed, *i.e.,* dripping status. To help understand the slag morphology change with wettability and flow behavior, the variation of average slag droplet circularity with time for different contact angles is generated, as shown in Figure 5.

The droplet's circularity, $C_{droplet}$, is defined as[62]

$$C_{\text{droplet}} = 4\pi A_{\text{droplet}} / P^2_{\text{droplet}} \quad [7]$$

$A_{droplet}$ and $P_{droplet}$ refer to the equivalent area and perimeter of a chosen droplet. Circularity values of 1.0 and approaching 0.0 indicate a perfect circle and an increasingly elongated polygon, respectively. Note that to avoid the effect of some tiny droplets hanging below the particles, droplets with circular radii less than 0.8 mm were not considered in the calculation of droplet circularity and relevant droplet size analysis.

Among all the tested contact angles, the circularity for the high wetting slag droplets is the lowest because this slag is more likely to flow over the particle surface. It also indicates that a wetting slag has a larger contact area with solid particles than non-wetting slag.

The variation of droplet circularity for a given contact angle is generally inversely proportional to the corresponding droplet size variation. To illustrate, for the non-wetting slag (θ = 157 deg), the lowest value of circularity corresponds to the largest droplet size (Figure 6). Hence, as the large droplets form in the base bed condition and subsequently flow through the bed, very deformed liquid rivulets can be formed.

Based on the above observations, two key factors affecting the indefinite-shaped slag in the base bed condition are the wettability and slag status such as static or dynamic holdup. Though beyond the scope of

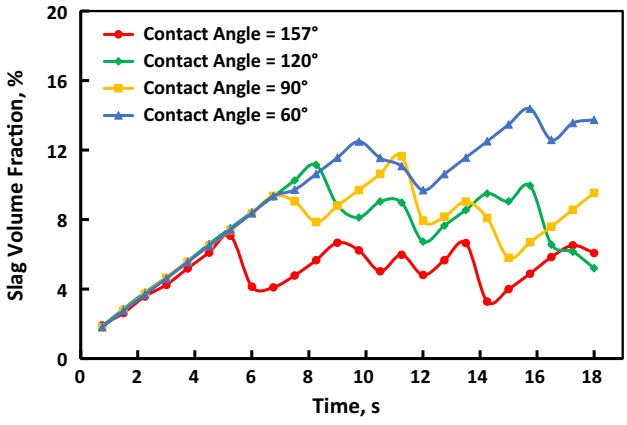

Fig. 4—Variation of slag volume fraction with time for different contact angles.

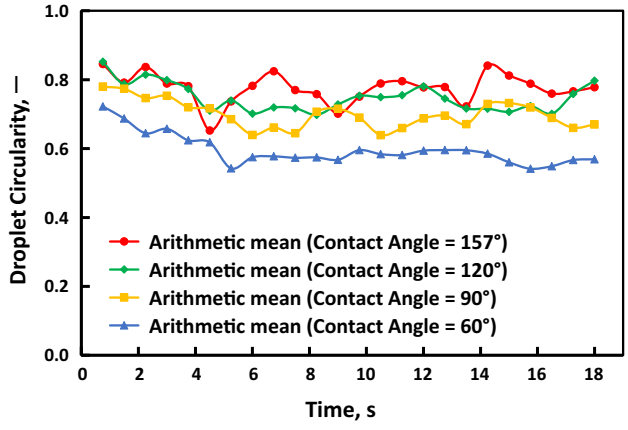

Fig. 5—Variation of average slag droplet circularity with time for different contact angles.

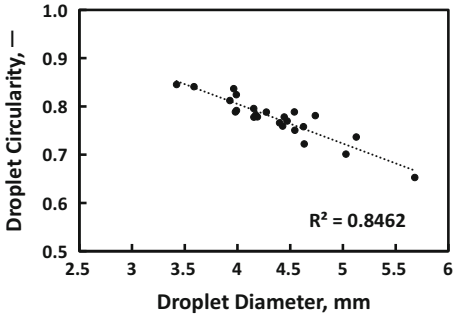

Fig. 6—Relation between droplet diameter and circularity for slag with a contact angle of 157 deg.

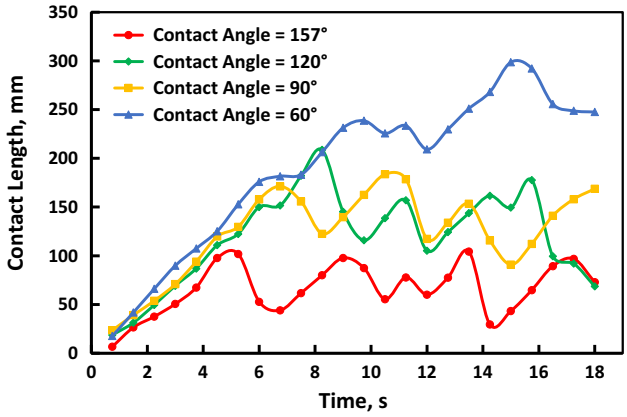

Fig. 7—Variation of contact area between slag and packing particles with time for different contact angles.

the current study, it is likely that particle size and shape will also affect droplet circularity. In this regard, caution should be exercised in applying the slag morphology to estimate the dripping or non-dripping status of slag.

3. *Contact length between slag and packing particles*

Figure 7 shows the variation of contact length between slag and packing particles. The current simulations were carried out under 2D conditions, so the contact "area" between slag and particle surface is represented by the contact length. The total contact length between slag and particle surface at time t, *i.e.*, L_t, can be obtained based on the following relationship,

$$L_t = \sum_{i=1}^{n} l_{x_i,t} \qquad [8]$$

where x_i is the i-th pixel at the interface between slag and particle surface, l is the pixel size, and n is the total number of pixels at the interface.

The interface between slag and particle surface at time t was identified based on the RGB value of each pixel in the image file outputted at time t. The image files are the same as snapshots shown in Figure 3.

The variation of contact length is generally consistent with the change of slag holdup (volume fraction) in Figure 4. The higher the slag volume fraction, the more likely slag is in contact with the particle surface. Both

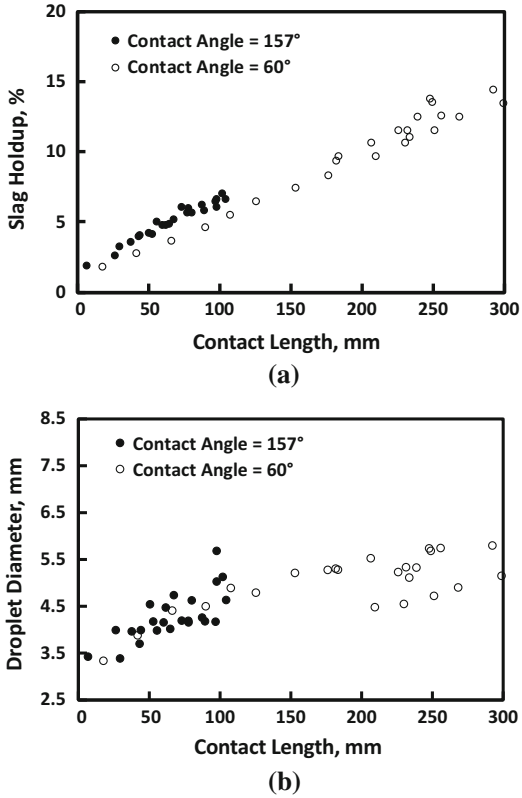

Fig. 8—(*a*) Relationship between slag holdup and contact length, and (*b*) relationship between slag droplet diameter and contact length, for different contact angles.

show the wetting condition enhances the contact length, *i.e.*, slag–solid interaction and reaction area increase with decreasing contact angle.

As shown in Figure 8, for the non-wetting slag (θ = 157 deg), both slag holdup and droplet size are proportional to contact length; for the wetting slag (θ = 60 deg), slag holdup remains proportional to contact length, but the relationship with droplet size is weak across the range of contact lengths. It is reasonable to propose the contact area represented by the contact length increases with more slag held up in the packed bed for both wetting and non-wetting slag. In the case of the wetting slag, holdup is higher. This indicates that the slag holdup could be used as a key indicator for the interaction contact area between slag and coke particles in the blast furnace.

4. *Effect of contact angles on drain curves*

Figure 9 compares macroscopic level trends/drain curves for different contact angles. As the flow changes from trickling (non-wetting slag) to creeping (wetting) flow, both total holdup and residence time of slag in the packed bed increase. As the wettability increases, *i.e.*, contact angle decreases, the starting time for slag flowing out of the packed bed is significantly delayed. It is noteworthy that the step changes in the drain curve are qualitatively consistent with experimental observations for non-wetting slag flow,[47] which is determined by the extent of slag accumulation in the packed bed.

5. *Evolution of slag held up in the gap between particles*

For the more wetting slag (θ = 60 deg), the evolution of slag in the gap between particles was closely tracked, as shown every 0.25 second in Figure 10. In Figure 10(a), the slag bridging between two particles could be treated as static holdup. However, in some respects, this holdup may not actually be "static." It may be replaced by the slag dripping from above, as demonstrated in Figures 10(a) through (f). It indicates that there are different states of static holdup in the bed, even only from the viewpoint of flow behavior. The amount of slag absorbed into the pore of particles or staying in dead spots of the packed bed is "inactive" static holdup. The amount of slag on the surface or simply bridging the particles is "active" static holdup, which could be continuously replaced by "new" slag. It is speculated that "active" static slag holdup occupies a high proportion of the total static holdup. It is evident that this part of slag has longer contact time with particles compared to dynamic holdup and can be also actively involved in the interaction with packed particles. Generally speaking, in the BF, this static holdup can contribute to the reaction between slag and coke, consumption of coke and slag transformation (primary to final slag). It is worth acknowledging that the exchange of "active" and "inactive" static holdup may occur as the overall situation changes such as the movement of coke bed or the change of slag wettability due to reactions.

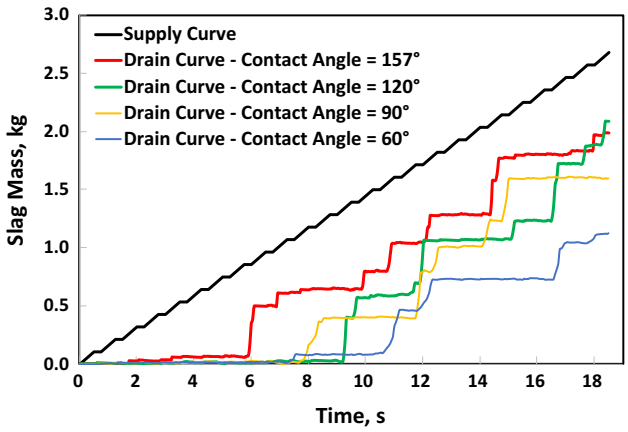

Fig. 9—Comparison of drain curves for different contact angles.

B. *Slag Flow in the Packed Bed with Poor Permeability Region*

In this section, the slag flow through a packed bed with (*a*) a central and (*b*) deadman-shaped poor permeability region is investigated.

1. *Central, poor permeability region*

A central, poor permeability region is mainly used to investigate the influence of varied packing structure. As introduced in Section II–B, only particle size is reduced in the central region, and the gap/opening between particles is narrower. The overall porosity in this region is the same as that in the uniform bed.

Figure 11 shows the simulated slag flow through this packed bed at 18 seconds. For a more non-wetting condition (θ = 157 deg), the results show slag bypassing the central region. With the decreased opening between particles, the slag easily accumulates above the poor permeability central region. Once the column of accumulated slag reaches a certain height, the slag finds another path *i.e.,* flow deviation occurs. Both our previous funnel experiments and simulations[27,36] support this flow blockage phenomenon.

As the contact angle decreases, the hydrostatic height to overcome the adhesive force between slag and solid particles is reached such that slag can flow into the central region. For example, as shown in Figure 11(d), the more wetting slag (θ = 60 deg) no longer bypasses the central region; instead, the slag flows into and through the central region, but with slower velocity. The increased spreading or dispersion of slag through this region is also more evident. From a gas permeability perspective, a wetting slag may more easily deteriorate a low permeability region through increased holdup. Moreover, the wetting condition also increases the chance of coke particles interacting with slag in a low permeability region.

Figure 12 further compares the four corresponding drain curves for a packed bed with a central, poor permeability region. The drain curve for the base bed and more non-wetting slag (θ = 157 deg) is provided for comparison.

Across the four slags, the more wetting (θ = 60 deg) causes the highest holdup and longest residence time. Compared to the base bed condition, all drain curves for a bed with a central poor permeability region show increased average holdup and residence time. Most of

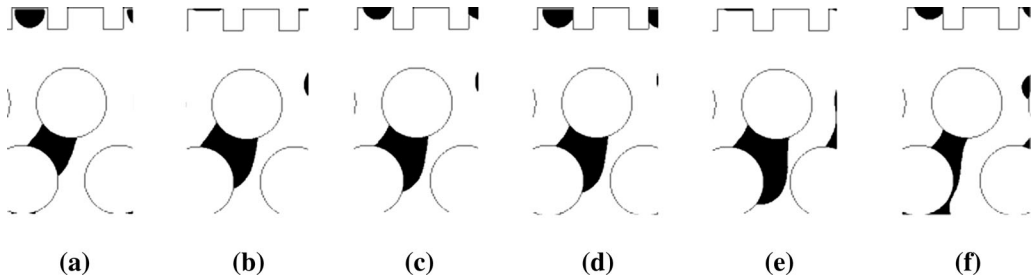

Fig. 10—Evolution of slag hold up in the gap at different times: (*a*) 13.5 s, (*b*) 13.75 s, (*c*) 14 s, (*d*) 14.25 s, (*e*) 14.5 s, and (*f*) 14.75 s.

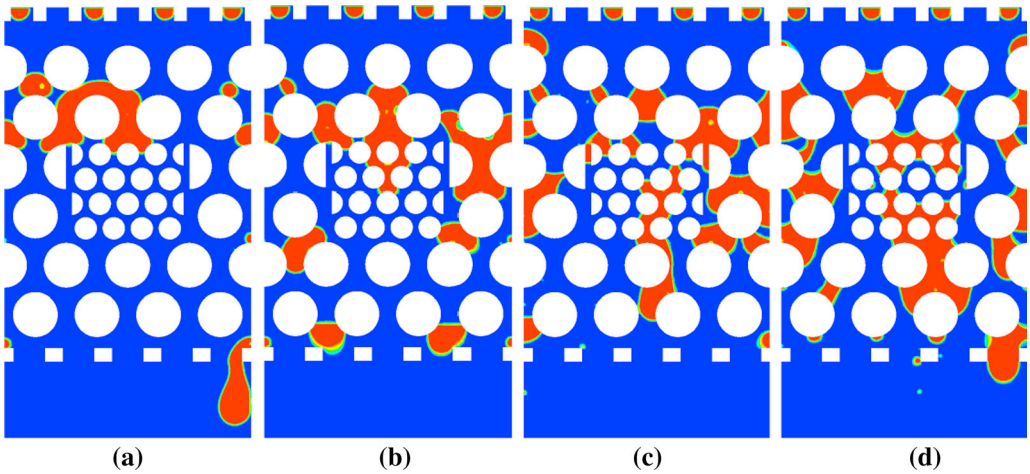

Fig. 11—Simulated slag flow in the packed bed with central region of poor permeability at time t = 18 s for different contact angles: (*a*) 157 deg, (*b*) 120 deg, (*c*) 90 deg, and (*d*) 60 deg.

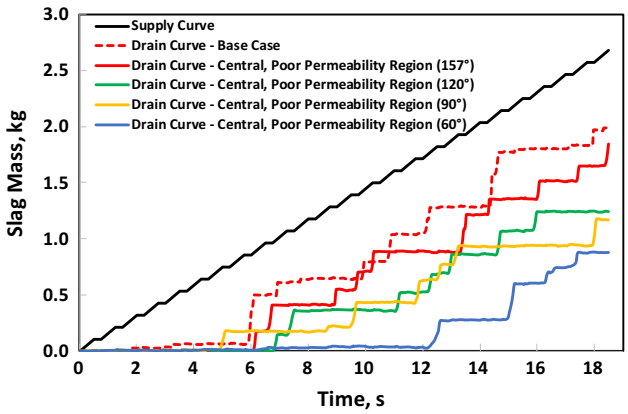

Fig. 12—Comparison of drain curves for the slag flow in the packed bed with central region of poor permeability.

these show a pattern of alternating long and then several short steps, which is likely due to variations in slag accumulation times, across different regions. The alternating pattern reflects different slag flow paths which overlap at the bottom outlet.

Overall, this type of macroscopic flow behavior can be used to infer the existence of non-uniform packing structures in HT experiments.[32] In the experiments, the local coke packing structure cannot be fully controlled, particularly for irregular coke particles. Hence, even though the overall bed porosity remains the same, it is observed that the drain curves experimentally obtained can be variable.

2. *Deadman-shaped poor permeability region*

To further investigate the effect of a poor permeability region on slag flow behavior, a bed with a deadman-shaped region [Figure 1(c)] was considered. In this deadman region, the overall porosity is the same as that in the base bed condition [Figure 1(a)].

The calculated slag flow fields at 18 seconds are shown in Figure 13. For the more non-wetting slag (θ = 157 deg), most of the slag flows around the deadman region, with higher slag holdups near the interface. As the contact angle decreases, slag can flow into the deadman region. In particular, the flow path for the more wetting slag (θ = 60 deg) appears stream-like rather than discrete droplets [Figure 13(d)]. Once flow paths have been formed, the slag prefers to flow along these paths because less energy is required. Beyond the deadman region, slag flows as discrete droplets. Similar observations have been reported elsewhere. Stream-like flow paths in a packed bed with particle size of 5 mm have been observed in LT experiments[19,21] using dyed water as the liquid phase with a contact angle of 65 deg; this was not the case for 10 mm particles. There is strong indication that steam-like flow in a packed bed is closely related to both particle morphology and liquid wettability.

Compared to the results with uniform packed bed in Figure 3, the capillary effect of slag flowing in the bed with poor permeability region is evident. For non-wetting slag, the capillary effect can be reflected by the overloading behavior or congestion at the packing surface of poor permeability region. For wetting slag, the slag enters the poor permeability region relatively easily, with dispersion evident.[63] However, gravity still plays a dominant role so that it is observed that slag flow is directional. Currently, the capillary constant (number)[64] based on gravity and surface tension, cohesive force, adhesive force in terms of the liquid-wall interaction, and complex flow path is inherently considered in the modeling. This determines the final flow behavior of slag in the packed bed.

Figure 14 shows the comparison of drain curves for the slag flow in the packed bed with the deadman-shaped, low permeability region. Within the 18 seconds time period, the more non-wetting slag (θ = 157 deg) presents higher holdup and longer residence time compared to the base bed result. However,

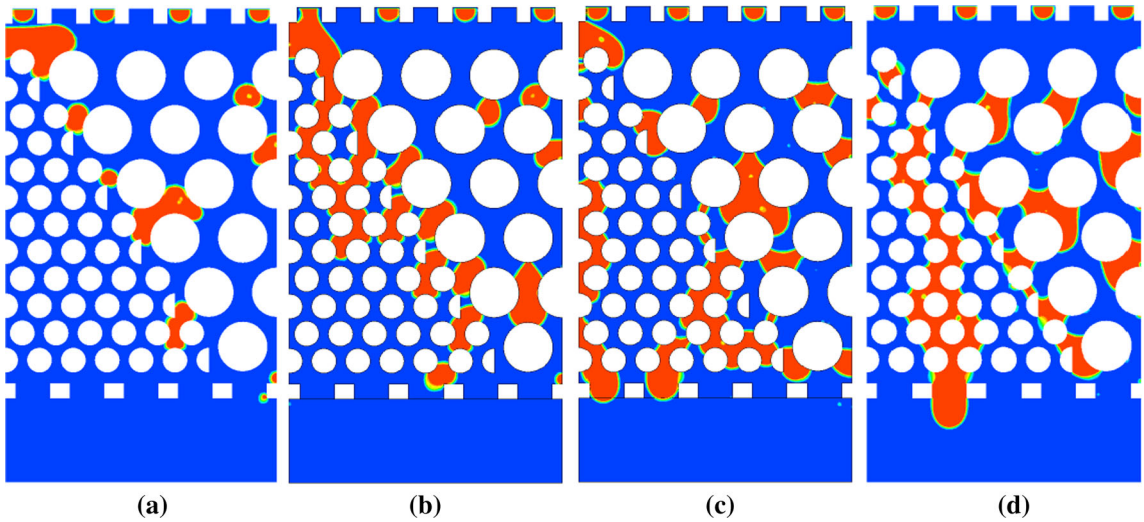

Fig. 13—Simulated slag flow in the packed bed with deadman-shaped poor permeability region at time t = 18 s for different contact angles: (*a*) 157 deg, (*b*) 120 deg, (*c*) 90 deg, and (*d*) 60 deg.

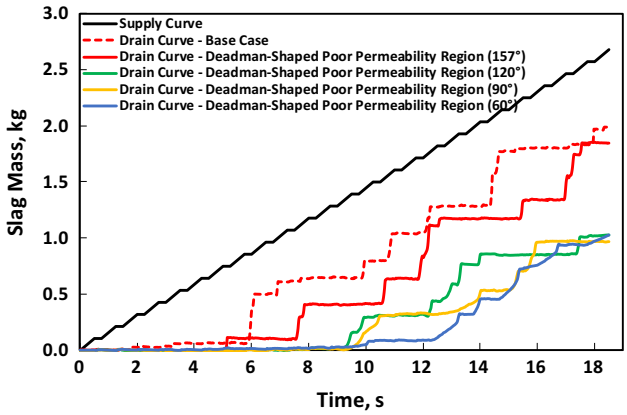

Fig. 14—Comparison of drain curves for the slag flow in the packed bed with deadman-shaped poor permeability region.

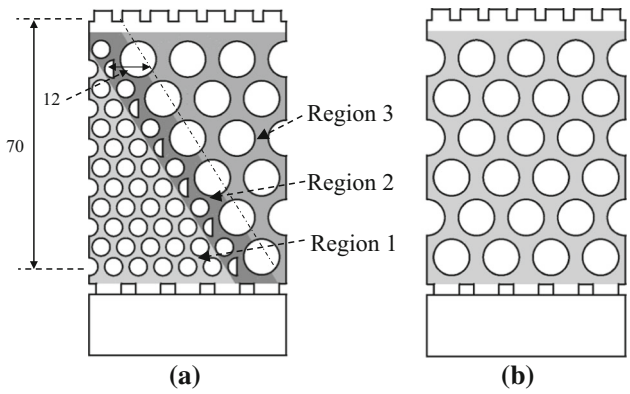

Fig. 15—Regions used to compare the variation of slag volume fraction (unit: mm): (*a*) sub-regions in the bed with deadman-shaped poor permeability region, and (*b*) base bed region.

compared to the other drain curves (which are not significantly different), this slag has the lowest holdup and shortest residence time.

To understand the effect of the poor permeability region on slag flow behavior, three sub-regions were analyzed [Figure 15(a)]: Region 1, the poor permeability region, representing an area of ~ 1332 mm^2; Region 2, across the surface of the poor permeability region, ~ 836 mm^2; and Region 3, beyond the poor permeability region, ~ 1684 mm^2. Region 2 includes one layer of small particles on the left side of the interface centerline and half of one layer of large particles on the right side. Figure 15(b) shows the base bed configuration.

The variation of slag volume fraction in different sub-regions is shown in Figure 16. The variation of slag volume fraction in the base bed region [Figure 15(b)] and base condition (Table III) is also provided for comparison.

Figure 16(a) shows that within the 18 seconds period, only a small volume of the more non-wetting slag (θ = 157 deg) flows into the poor permeability sub-region (Region 1). In the interface region (Region 2), the slag volume fraction is much higher. The variation of slag volume fraction outside the poor permeability region (Region 3) follows closely the trend for the base bed region and base condition.

Although the drain curves for other slags (θ = 120, 90, 60 deg) are relatively similar (Figure 14), the flow behaviors in the different sub-regions differ. In particular, for θ = 120 deg [Figure 13(b)], the slag volume fraction in Region 2 steadily increases from 10 seconds onwards. This is due to slag accumulation at the interface. As wetting increases, *e.g.*, θ = 90 deg, slag accumulation at the interface is less evident with more liquid entering Region 1. The slag distribution in the poor permeability region (Region 1) and its surface (Region 2) is similar.

From a gas permeability perspective, the above observations indicate that the more non-wetting slag is likely to only deteriorate the interface sub-region (Region 2) through reducing space for gas flow, while the more wetting slags deteriorate both the interface and internal region of poor permeability.

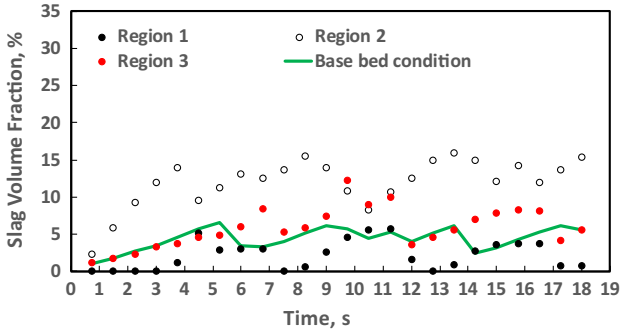

(a)

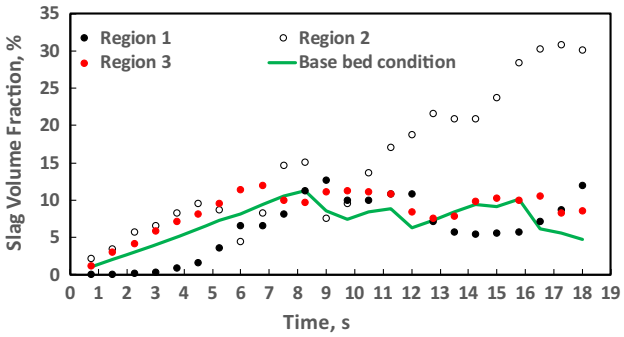

(b)

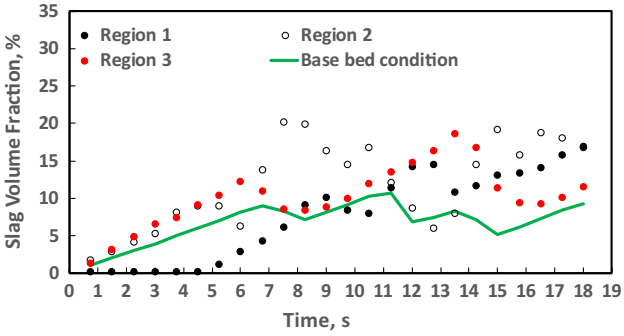

(c)

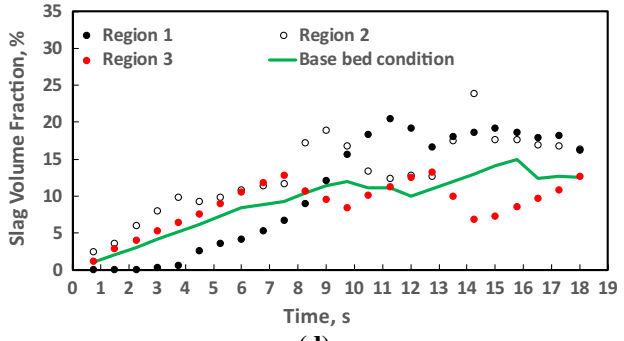

(d)

Fig. 16—Variation of slag volume fraction in the different region for different contact angles: (*a*) 157 deg, (*b*) 120 deg, (*c*) 90 deg, and (*d*) 60 deg.

3. *Slag flow in packed beds with different viscosities*

Figure 17 shows the slag flow field at time $t = 18$ seconds as the viscosity changes from the base value (0.264 Pa s) to four times this value (1.056 Pa s). The three previously described packed beds are investigated: base bed; bed with central region of poor permeability; and bed with deadman-shaped poor permeability region. The more non-wetting slag is used ($\theta = 157$ deg).

In the base bed condition, the residence time of slag in the upper part of bed increases as viscosity increases. Thus, it is easier for slag droplets to coalesce into large ones and total holdup increases. For the bed with a central region of poor permeability, both the base slag and high viscosity slag can bypass the central region. However, for the bed with a deadman-shaped region of poor permeability, a large amount of high viscosity slag can accumulate at the bed surface. Compared to the base condition, a high slag column can be formed in the case with high viscosity so that the hydrostatic pressure overcomes the bed resistance and the slag flows into the poor permeability region. In this regard, long stream-like flow paths can be observed in this region [Figure 17(f)]. In practice, particularly in the case of high PCR, it may be speculated that as the apparent viscosity of dripping slag increases due to, for example, assimilation of unburnt pulverized coal and/or fine coke, accumulated slag in the interface region may further deteriorate the gas permeability in the deadman.

A comparison of drain curves for the different beds (Figure 18) shows different starting points for slag flow out. For the base bed condition, the slag flows out of the bed relatively early. While the starting point for the bed with a central region of poor permeability is delayed, the subsequent transient flow is not significantly different compared with the base bed. These similar trends further illustrate the important role of hydrostatic pressure on the slag flow. Despite the deviated flow around the central region, large rivulets form and hydrostatic pressure increases to help accelerate the slag flow in the bed. For the bed with a deadman-shaped region of poor permeability, the larger area of poor permeability results in delayed slag flow, demonstrated by the large initial step in its drain curve.

4. *Potential application to BF lower zone conditions*

Though based on a 2D VOF modeling platform, the above simulation results and analysis provide new information concerning the influence of slag properties and coke bed condition on slag flow behavior in the BF lower zone.

This particle-scale information could have some practical relevance. For example, the consequence of large droplets of a higher viscosity slag formed in the coke bed and near the deadman (see Figure 17), and the stream-like flow paths that occur through the deadman with either a more wetting slag or a higher viscosity slag [see Figures 13(a) and 17(f)].

In the above case, the higher viscosity slag could promote gas channeling and the more wetting condition would more than likely enhance mass and heat transfer in specific regions of the lower zone. A higher viscosity and more wetting slag would also lead to higher slag holdup in the coke bed.

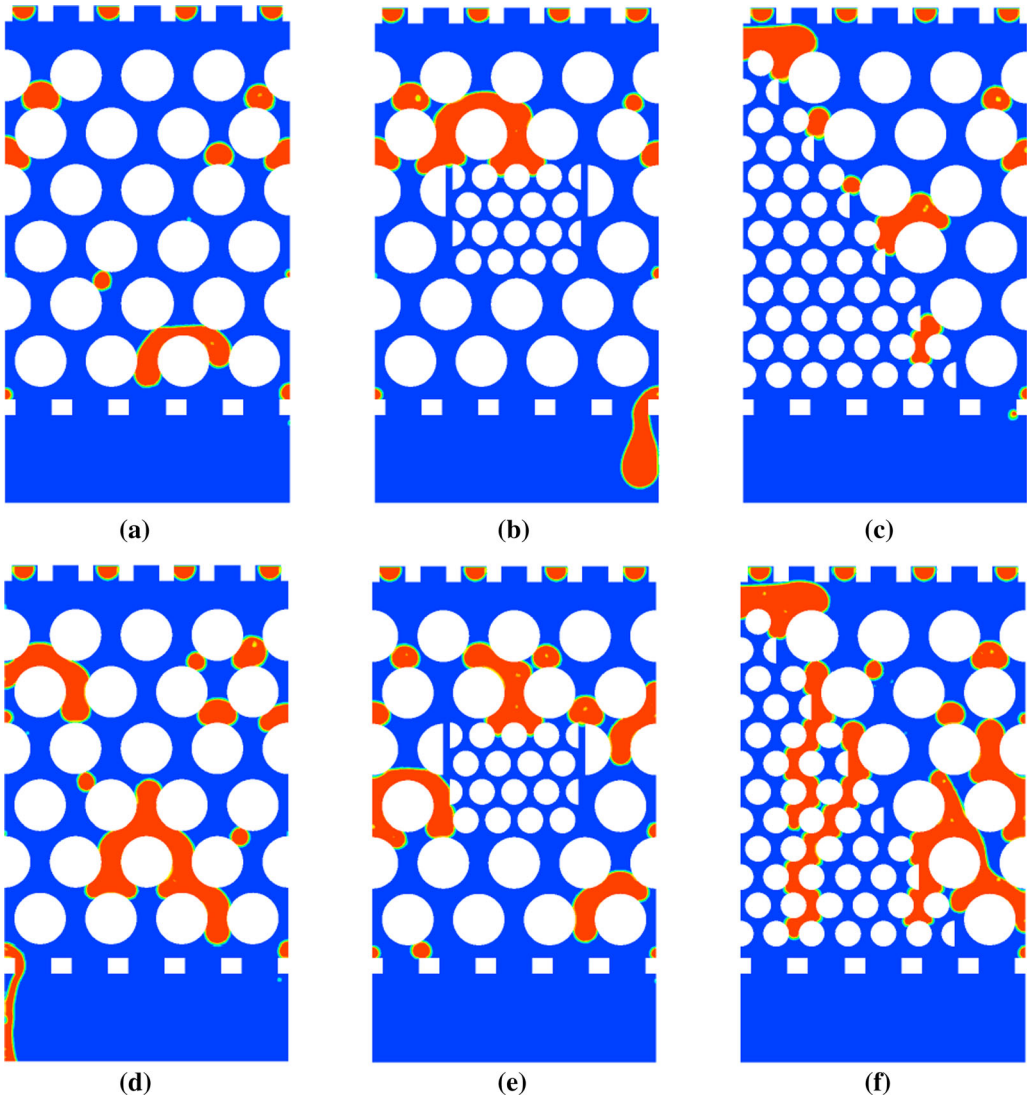

Fig. 17—Simulated slag flow with μ = 0.264 Pa·s for (*a*) to (*c*) and 1.056 Pa·s for (*d*) to (*f*), and in the different packed bed conditions: (a), (d) base bed; (b), (*e*) bed with central region of poor permeability; and (c), (f) bed with deadman-shaped poor permeability region.

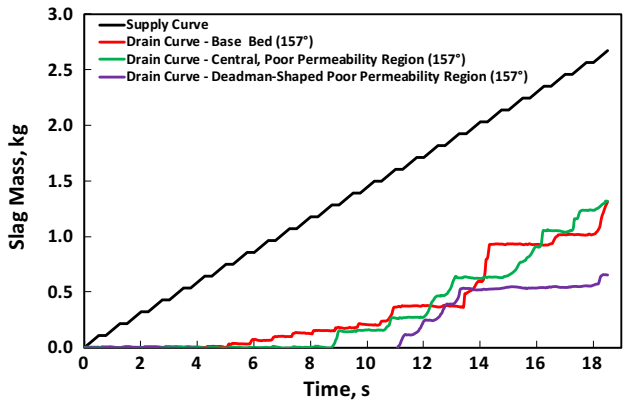

Fig. 18—Comparison of drain curves for slag flow in the packed bed with different-shaped poor permeability regions.

Furthermore, the easily formed high volume fraction of slag near the boundary between a permeable coke bed and a poor permeability region may, potentially, further deteriorate the permeability of the deadman and its surrounding region. In particular, this might occur for a slag trickling down through the dripping zone and assimilating remnant char or coke fines at high PCR.[5,65]

Overall, in terms of lower zone bed permeability and more generally, BF operational design, the modeling results suggest that a more non-wetting, less viscous slag is preferred for smooth flow behavior and hence, the target for slag design.

It should be noted that the above considerations are preliminary and are only taken from a slag flow perspective. In the future, heat transfer, slag–metal interaction, and chemical reactions in the lower part of BF should be investigated.

IV. CONCLUSIONS

Numerical investigation of slag flow behavior in a packed bed representing the lower zone of a BF was carried out considering more realistic and complex conditions such as bed permeability variations and more wide-ranging slag properties. A 2D VOF modeling technique was applied to track the movement of individual slag droplets in the packed bed. This modeling provided more detailed information at a mesoscopic level regarding the variation of slag droplets size, contact area, and trajectory, with less empirical correlations and assumptions necessary compared to traditional macroscopic modeling.

Results show that the variations in wettability, slag properties, and bed structure not only lead to changes in holdup and residence time of slag, but evidently, also generate different flow patterns in the packed bed. The key findings are summarized below:

- Different slag flow behaviors occurred with viscosity or slag wettability variations. More wetting conditions can cause a relatively uniform static holdup distribution; however, a higher viscosity slag results in the formation of large rivulets.
- A wetting slag flows along the profile of packing particles, showing a typical creeping flow. Compared to non-wetting slag flow, there are higher holdup, larger contact area between slag and particles, and lower circularity of slag droplets for a wetting slag flow.
- For regions of poor permeability, the flow direction of more non-wetting slags is altered, but not so for wetting slags. Changes in slag flow behavior were reflected in drain curves.
- Higher slag accumulation occurred at the upper surface (or interface) of the poor permeability region, particularly for more non-wetting slags.
- At a mesoscopic level, the slag flow is predominately linked to the formation of the liquid column, *i.e.,* the balance between static hydrostatic pressure and flow resistance due to adhesion.
- The indefinite shape of slag droplets becomes more pronounced in the case of higher slag holdup, larger droplet size, and a more highly wetting condition.
- Conceptually, slag static holdup is composed of "inactive and "active" static holdup, with the latter experiencing continuous replacement with "new" slag in the packed bed.
- Numerical results with different permeability regions highlight the significant influence of packing structure on the macroscopic flow behavior of slag, reflected by varied drain curves and blockage phenomena.

In order to obtain a better understanding of slag flow in the BF, these concluding remarks are suggested to be further verified under scaled-up and/or 3D simulation conditions and future experimental trials with different packing conditions and various primary/bosh/final slag compositions are also recommended to illuminate the physical flow behavior.

ACKNOWLEDGEMENTS

The authors acknowledge funding from the Australian Research Council (ARC) through the Industrial Transformation Research Hubs Scheme under Project Number: IH200100004. The funding support and permissions from ArcelorMittal and BlueScope Ltd to publish are gratefully acknowledged. This research was undertaken with the assistance of resources and services from the National Computational Infrastructure (NCI), which is supported by the Australian Government.

CONFLICT OF INTEREST

On behalf of all authors, the corresponding author states that there is no conflict of interest.

ABBREVIATIONS

A	Area, m^2
C	Circularity, –
F	Surface tension force, kg m^{-2} s^{-2}
G	Gravitational acceleration, m s^{-2}
l	Pixel size, mm
L_t	Total contact length between slag and particle surface at time t, mm
n	Total number of pixels at the interface, –
$\hat{n}_{iw}$	Unit vector normal to the wall, –
p	Pressure, Pa
P	Perimeter, mt Time, s
$\hat{t}_{iw}$	Unit vector tangential to the wall, –
u	Velocity, ms^{-1}
x_i	I-th pixel at the interface between slag and particle surface,

GREEK

ε_i	Volume fraction of phase i, -
θ_{iw}	Contact angle of phase i at the wall, Deg
κ_i	Curvature of the interface, m^{-1}
μ	Viscosity, kg m^{-1} s^{-1}
ρ	Density, kgm^{-3}
σ_{ij}	Surface tension between phases i and j, kgs^{-2}
τ	Stress tensor, Pa

SUBSCRIPTS

i	Phase i
j	Phase j
w	Wall

REFERENCES

1. Y. Omori: *Blast Furnace Phenomena and Modelling*, Elsevier Applied Science, London, 1987.
2. M. Sasaki, K. Ono, A. Suzuki, Y. Okuno, and K. Yoshizawa: *Trans. Iron Steel Inst. Jpn.*, 1977, vol. 17, pp. 391–400.
3. A.K. Biswas: *Principles of Blast Furnace Ironmaking*, Cootha Publishing House, Brisbane, 1981.
4. M. Geerdes, H. Toxopeus, and C. Vliet: *Modern Blast Furnace Ironmaking: An Introduction*, 2nd ed. IOS Press, Amsterdam, 2009.
5. M. Ichida, T. Orimoto, T. Tanaka, and F. Koizumi: *ISIJ Int.*, 2001, vol. 41, pp. 325–32.
6. P.A. Tanskanen, S.M. Huttunen, P.H. Mannila, and J.J. Härkki: *Ironmak. Steelmak.*, 2002, vol. 29, pp. 281–86.
7. K.O. Jang, X. Ma, J. Zhu, H. Xu, G. Wang, and B. Zhao: *Metall. Mater. Trans. B.*, 2017, vol. 48B, pp. 1547–60.
8. L. Baussaron, C. Julcour-Lebigue, A.M. Wilhelm, H. Delmas, and C. Boyer: *AIChE J.*, 2007, vol. 53, pp. 1850–60.
9. K. Li, J. Zhang, Z. Liu, M. Barati, J. Zhong, M. Wei, G. Wang, K. Jiao, and T. Yang: *Metall. Mater. Trans. B.*, 2015, vol. 46B, pp. 1104–11.
10. T. Usui, H. Kawabata, Z.I. Morita, and K. Masamori: *ISIJ Int.*, 1993, vol. 33, pp. 687–96.
11. T. Sugiyama, T. Nakagawa, H. Sibaike, and Y. Oda: *Tetsu to Hagane*, 1987, vol. 73, pp. 2044–51.
12. J.F. Elliott, R.A. Buchanan, and J.B. Wagstaff: *J. Metals*, 1952, vol. 194, pp. 709–17.
13. J. Szekely and J. Mendrykowski: *Chem. Eng. Sci.*, 1972, vol. 27, pp. 959–63.
14. N. Standish and J.B. Drinkwater: *J. Metals*, 1972, vol. 24, pp. 43–45.
15. T. Fukutake and V. Rajakumar: *Trans. Iron Steel Inst. Japan*, 1982, vol. 22, pp. 355–64.
16. T.S. Pham, D. Pinson, A.B. Yu, and P. Zulli: *Chem. Eng. Sci.*, 1999, vol. 54, pp. 5339–45.
17. G.S. Gupta, J.D. Litster, V.R. Rudolph, E.T. White, and A. Domanti: *ISIJ Int.*, 1996, vol. 36, pp. 32–39.
18. S.J. Chew, G.X. Wang, A.B. Yu, and P. Zulli: *Ironmak. Steelmak.*, 1997, vol. 24, pp. 392–400.
19. H. Kawabata, K. Shinmyou, T. Harada, and T. Usui: *ISIJ Int.*, 2005, vol. 45, pp. 1474–81.
20. Y. Bando, S. Hayashi, A. Matsubara, and M. Nakamura: *ISIJ Int.*, 2005, vol. 45, pp. 1461–65.
21. H. Kawabata, Z. Liu, F. Fujita, and T. Usui: *ISIJ Int.*, 2005, vol. 45, pp. 1466–73.
22. M. Li, Y. Bando, T. Tsuge, K. Yasuda, and M. Nakamura: *Chem. Eng. Sci.*, 2001, vol. 56, pp. 5969–76.
23. D.Y. Liu, G.X. Wang, and J.D. Litster: *AIChE J.*, 2002, vol. 48, pp. 953–62.
24. Y. Eto, K. Takeda, S. Miyagawa, H. Itaya, and S. Taguchi: *ISIJ Int.*, 1993, vol. 33, pp. 681–86.
25. D. Jang, M. Shin, J.S. Oh, H.S. Kim, S.H. Yi, and J. Lee: *ISIJ Int.*, 2014, vol. 54, pp. 1251–55.
26. M. Hayashi, S. Sukenaga, K.I. Ohno, S. Ueda, K. Sunahara, and N. Saito: *Tetsu-To-Hagane*, 2014, vol. 100, pp. 211–26.
27. H.L. George, B.J. Monaghan, R.J. Longbottom, S.J. Chew, and P.R. Austin: *ISIJ Int.*, 2013, vol. 53, pp. 1172–79.
28. H. Ohgusu, Y. Sassa, Y. Tomita, K. Tanaka, and M. Hasegawa: *Tetsu to Hagane*, 1992, vol. 78, pp. 1164–70.
29. W.M. Husslage, M.A. Reuter, R.H. Heerema, T. Bakker, and A.G.S. Steeghs: *Metall. Mater. Trans. B.*, 2005, vol. 36B, pp. 765–76.
30. I.H. Jeong, H.S. Kim, and Y. Sasaki: *ISIJ Int.*, 2013, vol. 53, pp. 2090–98.
31. H.L. George, R.J. Longbottom, S.J. Chew, D.J. Pinson, and B.J. Monaghan: *ISIJ Int.*, 2014, vol. 54, pp. 1790–96.
32. H.L. George, R.J. Longbottom, S.J. Chew, and B.J. Monaghan: *ISIJ Int.*, 2014, vol. 54, pp. 820–26.
33. J.S. Oh and J. Lee: *J. Mater. Sci.*, 2016, vol. 51, pp. 1813–19.
34. M. Hino, T. Nagasaka, A. Katsumata, K.-I. Higuchi, K. Yamaguchi, and N. Kon-No: *Metall. Mater. Trans. B.*, 1999, vol. 30B, pp. 671–83.
35. D.D. Geleta, M.I.H. Siddiqui, and J. Lee: *Metall. Mater. Trans. B*, 2020, vol. 51B, pp. 102–13.
36. X.F. Dong, A. Jayasekara, D. Sert, R. Ferreira, P. Gardin, B.J. Monaghan, S.J. Chew, D. Pinson, and P. Zulli: *Metall. Mater. Trans. B.*, 2021, vol. 52B, pp. 255–66.
37. T. Kon, S. Natsui, S. Ueda, R. Inoue, and T. Ariyama: *ISIJ Int.*, 2012, vol. 52, pp. 1565–73.
38. T. Kon, S. Natsui, S. Ueda, R. Inoue, and T. Ariyama: *ISIJ Int.*, 2013, vol. 53, pp. 590–97.
39. T. Kon, S. Natsui, S. Ueda, and H. Nogami: *ISIJ Int.*, 2015, vol. 55, pp. 1284–90.
40. S. Natsui, T. Kikuchi, R.O. Suzuki, T. Kon, S. Ueda, and H. Nogami: *ISIJ Int.*, 2015, vol. 55, pp. 1259–66.
41. S. Natsui, K.I. Ohno, S. Sukenaga, T. Kikuchi, and R.O. Suzuki: *ISIJ Int.*, 2018, vol. 58, pp. 282–91.
42. S. Natsui, K. Tonya, H. Nogami, T. Kikuchi, R.O. Suzuki, K.I. Ohno, S. Sukenaga, T. Kon, S. Ishihara, and S. Ueda: *Processes*, 2020, vol. 8, pp. 221–34.
43. S. Natsui, A. Sawada, H. Nogami, T. Kikuchi, and R.O. Suzuki: *ISIJ Int.*, 2020, vol. 60, pp. 1445–52.
44. S. Natsui, A. Sawada, H. Nogami, T. Kikuchi, and R.O. Suzuki: *ISIJ Int.*, 2020, vol. 60, pp. 1453–60.
45. S. Natsui, K. Tonya, A. Hirai, and H. Nogami: *Chem. Eng. J.*, 2021, vol. 414, p. 128606.
46. S. Natsui, K. Tonya, H. Nogami, T. Kikuchi, and R.O. Suzuki: *Chem. Eng. Sci.*, 2021, vol. 229, p. 116035.
47. X.F. Dong, A. Jayasekara, D. Sert, R. Ferreira, P. Gardin, B.J. Monaghan, S.J. Chew, D. Pinson, and P. Zulli: *Metall. Mater. Trans. B.*, 2021, vol. 52B, pp. 2926–38.
48. T. Sugiyama and M. Sugata, *Nippon Steel Technical Report* 1987, pp. 32–42.
49. J. Szekely and Y. Kajiwara: *Trans. Iron Steel Inst. Jpn.*, 1979, vol. 19, pp. 76–84.
50. J. Wang, R. Takahashi, and J. Yagi: *Tetsu to Hagane*, 1991, vol. 77, pp. 1585–92.
51. G.X. Wang, S.J. Chew, A.B. Yu, and P. Zulli: *Metall. Mater. Trans. B.*, 1997, vol. 28B, pp. 333–43.
52. G.X. Wang, S.J. Chew, A.B. Yu, and P. Zulli: *ISIJ Int.*, 1997, vol. 37, pp. 573–82.
53. S.J. Chew, P. Zulli, and A. Yu: *ISIJ Int.*, 2001, vol. 41, pp. 1112–21.
54. J.J. Monaghan: *Comput. Phys. Commun.*, 1988, vol. 48, pp. 89–96.
55. J.J. Monaghan, In *Annual Review of Astronomy and Astrophysics*, (1992), pp. 543–74.
56. C.W. Hirt and B.D. Nichols: *J. Comput. Phys.*, 1981, vol. 39, pp. 201–25.
57. V.K. Gupta, K. Srikanth and H. Punekar, *2016 IEEE 23rd International Conference on High Performance Computing Workshops*, Hyderabad, 2016, pp. 100–105.
58. D.G. Holmes and S.D. Connell, *9th Computational Fluid Dynamics Conference*, Buffalo, NY, 1989.
59. K.C. Mills: *Slags Model (ed 1.07)*. National Physical Laboratory, UK, 1991.
60. P.V. Riboud, Y. Roux, L.D. Lucas, and H. Gaye: *Fachberichte Huttenpraxis Metallweiterverarbeitung*, 1981, vol. 19, pp. 859–69.
61. T.W. Kang, S. Gupta, N. Saha-Chaudhury, and V. Sahajwalla: *ISIJ Int.*, 2005, vol. 45, pp. 1526–35.
62. E.P. Cox: *J. Paleontol.*, 1927, vol. 1, pp. 179–83.
63. K. Lappalainen, M. Manninen, and V. Alopaeus: *Chem. Eng. Sci.*, 2009, vol. 64, pp. 207–18.
64. B.E. Rapp: *Microfluidics: Modeling, Mechanics and Mathematics*, Elsevier, Amsterdam, 2017.
65. R. Murai, A. Murao, K. Goto, M. Sato, and T. Ariyama: *Tetsu-To-Hagane*, 2002, vol. 88, pp. 249–55.